Anal Bioanal Chem (2017) 409:6379–6386
DOI 10.1007/s00216-017-0577-2

RESEARCH PAPER

Functionalization of MgZnO nanorod films and characterization by FTIR microscopic imaging

Yuan Chen[1] · Qihong Zhang[1] · Carol Flach[1] · Richard Mendelsohn[1] · Elena Galoppini[1] · Pavel Ivanoff Reyes[2] · Keyang Yang[2] · Rui Li[2] · Guangyuan Li[2] · Yicheng Lu[2]

Received: 7 April 2017 / Revised: 22 July 2017 / Accepted: 8 August 2017 / Published online: 24 August 2017

Abstract Metal organic chemical vapor deposition grown films consisting of $Mg_xZn_{1-x}O$ ($4\% < x < 5\%$) nanorod arrays ($MgZnO_{nano}$) were functionalized with 11-azidoundecanoic acid (**1**). The $MgZnO_{nano}$ was used instead of pure ZnO to take advantage of the etching resistance of the $MgZnO_{nano}$ during the binding and subsequent sensing device fabrication processes of sensor devices, while the low Mg composition level ensures that selected ZnO properties useful for sensors development, such as piezoelectricity, are retained. Compound **1** was bound to the $MgZnO_{nano}$ surface through the carboxylic acid group, leaving the azido group available for click chemistry and as a convenient infrared spectroscopy (IR) probe. The progress of the functionalization with **1** was characterized by FTIR microscopic imaging as a function of binding time, solvents employed, and $MgZnO_{nano}$ morphology. Binding of **1** was most stable in solutions of 3-methoxypropionitrile (MPN), a non-protic polar solvent. This occurred first in μm-scale islands, then expanded to form a rather uniform layer after 22 h. Binding in alcohols resulted in less homogenous coverage, but the **1**/$MgZnO_{nano}$ films prepared from MPN were stable upon treatment with alcohols at room temperature. The binding behavior was significantly dependent on the surface morphology of $MgZnO_{nano}$.

Keywords Zinc oxide · Magnesium zinc oxide · Surface functionalization · FTIR microscopic imaging

Introduction

Nanostructured zinc oxide (ZnO_{nano}) films grown on a variety of substrates and functionalized with redox-active molecules, chromophores, or biomolecules have been the object of intense research activity, both experimentally and theoretically [1–3], for over a decade, because they are key components of photovoltaics [4–6], catalysts [7, 8], and sensors [9–12]. The ability of ZnO to form highly ordered nanostructure arrays, combined with its multifunctional properties, is particularly advantageous. For instance, chromophores bound to nanostructured ZnO films were used to probe the specific role of ZnO and its morphologies on electron injection [13, 14], electron transport [15, 16], and electronic coupling [17].

Vertically aligned, highly crystalline ZnO nanorods grown by metal organic chemical vapor deposition (MOCVD) are excellent platforms to develop novel biochemical sensing devices, as they combine bio-compatibility with its intrinsic multifunctional properties. In addition, through precise control of doping during the MOCVD growth process, these films can be made optically transparent and conductive [18], piezoelectric [19, 20], or ferromagnetic [21, 22]. Due to the significantly higher surface area, sensors made from ZnO_{nano} films grown by MOCVD on quartz crystal microbalance (QCM) exhibited much higher loading effect compared to that made by nanospheres [23].

A prerequisite that is necessary for practical biosensing applications of nanostructured ZnO films is the ability to control and characterize the molecule binding process on ZnO_{nano} surfaces

Electronic supplementary material The online version of this article (doi:10.1007/s00216-017-0577-2) contains supplementary material, which is available to authorized users.

✉ Elena Galoppini
galoppin@newark.rutgers.edu

✉ Yicheng Lu
ylu@soe.rutgers.edu

[1] Department of Chemistry, Rutgers, The State University of New Jersey, 73 Warren Street, Newark, NJ 07102, USA

[2] Department of Electrical and Computer Engineering, Rutgers, The State University of New Jersey, Piscataway, NJ 08854, USA

[24]. As a part of our keen interest in developing highly selective ZnO_{nano}-based biochemical sensors, we first developed binding techniques for several anchor groups [25]. Subsequently, we described the step-wise functionalization of MOCVD-grown ZnO_{nano} by binding a saturated alkyl linker with a COOH anchor group on one end, and capped on the other end with a functional group ready to undergo substitution reactions [23] or azide-alkyne click chemistry [26]. Through these methods, we bound fluorophores as well as biomolecules [27]. This interfacial chemistry improved control of the organic molecule/ZnO_{nano} layer, resulting in highly selective and sensitive sensing functions [28]. However, the pure ZnO_{nano} films are easily etched, limiting their stability and application for biochemical sensing. Furthermore, the use of fluorescent tags was needed to carry out the characterization of the binding by fluorescence microscopy, since FT-IR-ATR spectra used for thin (~ 0.5 μm) films generally result in poor quality resolution, and cannot reveal the binding distribution on a large area of the film.

In this paper, we describe the use of FTIR microscopic imaging to characterize and monitor the binding process. FTIR microscopic imaging techniques, whereas widely used in biophysics studies [29], have not been employed in metal oxide surface binding studies. Second, we employed ternary nanostructured $Mg_xZn_{1-x}O$ ($4\% < x < 5\%$) ($MgZnO_{nano}$), because it possesses all the advantageous intrinsic material properties of ZnO but exhibits increased resistance to acids [30], including the COOH group, which remains the most effective and common anchor group for ZnO. Etching of ZnO nanorods and nanoparticle films to form zincate salts, and the dependence on pH, binding time and concentration of the binding solution, have been widely documented [31–33]. Third, we bound a bifunctional linker, 11-azidoundecanoic acid (**1**), to the surface through the carboxylic acid group, leaving the azido group available for click chemistry and as a convenient IR probe. Finally, we used 3-methoxypropionitrile as a polar, non-protic solvent as well as an excellent binding medium that retains the bound molecular layer. Herein, solvent effects were also studied by FTIR microscopic imaging.

The ability to obtain a homogeneous, closely packed, reactive layer in a highly reproducible manner is extremely important for biomolecule immobilization. In this paper, we address improved binding methods, as well as an effective characterization of the functionalized layer in the absence of fluorescent probes. These results pave the way for a general, reproducible approach towards robust, homogenous organic layers on $MgZnO_{nano}$, ready for further reactivity, and demonstrate the use of IR imaging for this type of application.

Experimental

$MgZnO_{nano}$ films growth $MgZnO_{nano}$ films were grown on C-plane sapphire (c-Al_2O_3) (Saint-Gobain Crystals, 430 μm, (0001)) substrates using Metal Organic Chemical Vapor Deposition (MOCVD) at 450–500 °C. Diethylzinc (DEZn) (Rohm and Haas, 99.999%), bis-(methyl-cyclopentadienyl) magnesium (MCp_2Mg) (Rohm and Haas, 99.999%) and ultra-high purity (99.999%) oxygen gas were used as the Zn and Mg metalorganic source and oxidizer, respectively. Ultra-high purity (99.999%) argon was used as the carrier gas. The thicknesses of $MgZnO_{nano}$ films used in this work ranged from 0.50 to 1.0 μm. Mg composition x in $Mg_xZn_{1-x}O$ was kept in 4–5% for all films, and it was estimated using optical transmission spectroscopy (see Electronic Supplementary Material (ESM) Fig. S11 and Fig. S12). Since Mg composition is low in the ternary compound, the MgZnO crystal structure remains to be Wurtzite, the same as that of ZnO (see ESM Fig. S1 ([34])).

General All the following solvents and reagents were used as received from commercial sources: 3-methoxypropionitrile (MPN) (99%), 1-butanol (≥ 99.4%), ethyl alcohol (≥ 99.5%), *N,N*-dimethylformamide (anhydrous, 99.8%), dichloromethane (≥ 99.5%), 11-bromoundecanoic acid (99%), and sodium azide (99%). The reactions were performed under N_2 gas and in oven-dried glassware. ^1H and ^{13}C nuclear magnetic resonance (NMR) spectra were collected on a Varian NMR spectrometer operating at 599.714 Hz for ^1H and 150.812 Hz for ^{13}C. Chemical shifts (δ) are reported relative to the central line of the solvent: $CDCl_3$ (δ 7.27 ppm for ^1H and δ 77.27 ppm for ^{13}C), and spin-spin coupling constants (J) are reported in Hz. The Fourier transform infrared (FTIR) spectrum in Fig. 1 (red line) was collected on a Thermo Electron Corporation Nicolet 6700 FTIR utilizing the SMART MIRacle-single bounce ATR accessory (ZnSe crystal, with 128 scans and spectral resolution of 8 cm^{-1}). Field emission scanning electron microscopy (FESEM) images were collected on a Hitachi S4800. ESI spectra were collected on an Apex-ultra 70 hybrid Fourier transform mass spectrometer (Bruker Daltonics).

Synthesis of 11-azidoundecanoic acid (1) 11-azidoundecanoic acid was synthesized by minor modification of a published procedure [26]. Sodium azide (0.50 g, 7.7 mmol) was added to a solution of 11-bromoundecanoic acid (1.00 g, 3.8 mmol) in DMF (5 ml) while stirring. The reaction mixture was heated at 80 °C for 3 h, then diluted with CH_2Cl_2 (25 ml), and washed by gently stirring with diluted (0.1 N) aqueous HCl solution. The organic layer was dried over Na_2SO_4 and evaporated in vacuo to yield a pale yellow oil (0.70 g, 3.1 mmol, 80%). ^1H NMR ($CDCl_3$) δ 10.08 (br, 1H), 3.26 (t, J = 7.2, 2 H), 2.35 (t, J = 7.8, 2 H), 1.66–1.57 (m, 4H), 1.39–1.29 (m, 12H). ^{13}C NMR ($CDCl_3$) δ 180.26, 51.38, 34.31, 29.68, 29.59, 29.48, 29.41, 29.32, 29.13, 26.99, 24.95 (see ESM Fig.S9 and Fig.S10) *CAUTION*: organic azides and sodium azide may decompose explosively. Azide waste should not come in contact with concentrated acids or metals.

Binding of 11-azidoundecanoic acid (1) onto $MgZnO_{nano}$ film (droplet method) A small volume (5 drops) of a 10-mM solution of **1** (either 2:1 1-butanol/ethanol or 3-methoxypropionitrile) was deposited onto a pristine $MgZnO_{nano}$ film grown on a sapphire substrate placed flat in a glass Petri dish, which was then sealed to prevent evaporation. After reacting for the indicated period of time (between 0.5 h to about 2 days, see Results and Discussion), the film was thoroughly rinsed with neat solvent to remove weakly bound or physisorbed molecules, and then dried under gentle nitrogen flow.

FTIR microscopic imaging and data analysis [29] FTIR microscopic images of $MgZnO_{nano}$ films were collected with a Perkin-Elmer Spotlight 300 system (Perkin Elmer Life and Analytical Science, Inc., Waltham, MA) in the transmission mode with an essentially linear array (16 × 1) of mercury-cadmium-telluride (MCT) detector elements. Imaging size was 200 × 200 μm^2. Images were collected with a 6.25 × 6.25 μm^2 pixel size and 32 scans at a spectral resolution of 8 cm^{-1}, corresponding to 32 × 32 pixel images. Visible micrographs were obtained with the optical microscope integrated into the Spotlight 300 system. FTIR microscopic images were generated from FTIR spectral data using ISys 3.1 software (Malvern Instruments, UK). Image planes of integrated band area were produced after linear baselines were applied in spectral regions of interest. The scale bar is color coded and selected to display the corresponding integrated area (±STD) above the detection limit to highlight differences upon treatments. The films used in our study were fixed onto a plate prior to data acquisition. Small shifts may occur during this process, resulting in small (~ μm scale) shifts of the images obtained.

Results and discussion

The functionalization of $MgZnO_{nano}$ films with 11-azidoundecanoic acid (**1**) is illustrated in Scheme 1. In the schematic, the bifunctional linker (**1**) is shown binding to $MgZnO_{nano}$ film through the COOH group, leaving the azido functional group available for click reaction with other molecules or biomolecules. In our study, the azido group also serves as a IR tag.

The binding process was monitored by IR imaging. Spectra of neat **1** and **1**/MgZnO are shown in Fig. 1 to illustrate the characteristic spectral changes that take place upon binding. The spectral range was limited to the 4000–1400 cm^{-1} region due to the intense background of the MgZnO/c-sapphire films. The azido group in **1** has a characteristic, intense asymmetric stretching (ν_{as}(N = N = N)) band at 2096 cm^{-1}, which serves as an IR tag. This band shifted to 2130 cm^{-1} after binding onto $MgZnO_{nano}$.

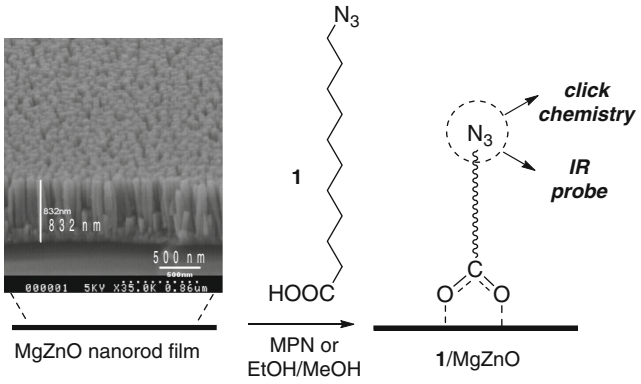

Scheme 1 Scheme of the functionalization of $MgZnO_{nano}$ film

The COOH group undergoes characteristic spectral changes upon binding, similar to those observed for binding to other nanostructured metal oxides [25]. The broad OH stretching band (ν(O-H)) observed over the 3300–2500 cm^{-1} region and the carbonyl stretching band (ν(C = O)) at 1706 cm^{-1} of the free acid disappeared, and new bands near 1540 cm^{-1} emerged, revealing the presence of a carboxylate moiety [23]. Overall, the spectral changes of the COOH group and the presence of the ν_{as}(N = N = N) band are consistent with covalent binding through the COOH group. By imaging the integrated area under the azide (2212–2064 cm^{-1}) or carboxylate (1564–1480 cm^{-1}) bands, we can evaluate the distribution of the bound 11-azidoundecanoic acid molecules. Additional observations in the C-H stretching region (2800–3000 cm^{-1}) are strongly suggestive of binding. The methylene stretching bands (asymmetric, ν_{as} CH_2 at ~ 2920 cm^{-1} and symmetric, ν_s CH_2 at ~ 2850 cm^{-1}) arise from the acyl chain of linker **1** and display downward frequency shifts upon

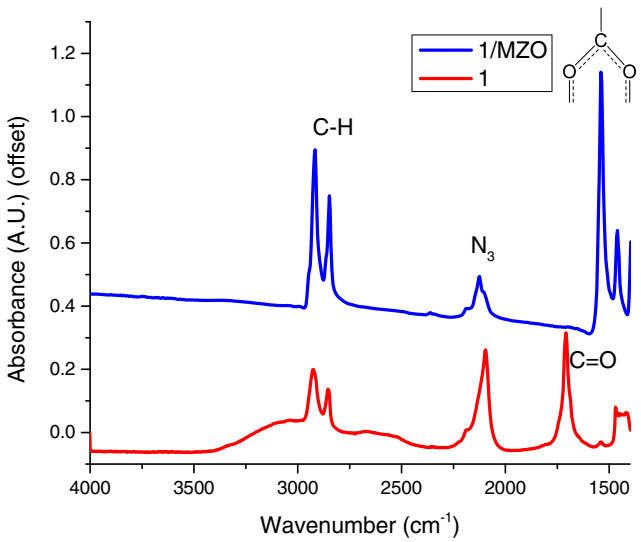

Fig. 1 FTIR-ATR spectrum of neat 11-azidoundecanoic acid (**1**) (bottom, red line) and representative single pixel FTIR spectrum of **1**/$MgZnO_{nano}$ (top, blue line)

binding. The ν_{as} CH_2 band shifts from ~ 2925 to 2916 cm^{-1} whereas the ν_s CH_2 band shifts from ~2854 to 2848 cm^{-1}. These shifts indicate that an increase in the alkyl chain conformational order and packing has occurred upon binding [35, 36]. Compared to the state of the alkyl chains in solution, it is likely that they become more ordered and closely packed on the surface of the nanorod films.

Using IR imaging, we probed the influence of the solvent employed for the binding solution, the binding time, and the morphology of the $MgZnO_{nano}$ on the uniformity of the **1**/MgZnO layer and on the binding process. IR maps were obtained by collecting spectra from nine different areas of each film (200 × 200 μm^2 each) (see ESM Fig. S2). The IR images were generated by integrating the area of two selected bands of interest, specifically the $\nu_{as}(N_3)$ at 2212–2064 cm^{-1}, and the $\nu_{as}(O\underline{\ddot{}}C\underline{\ddot{}}O)$ at 1564–1480 cm^{-1}, after baseline correction. The detection limit, based on a signal to noise ratio of 3, was 0.19 for the azide band and 0.68 for the carboxylate moiety. Regions below the detection limit were displayed in white.

The spectral shifts upon binding and presence of shoulders in the main azide band that we have observed in this experiment and in the prior work [24] deserve a comment. We think that these changes and the presence of shoulders likely arise from differences in local environments, both in the neat sample of **1** and on **1**/MgZnO. Regarding the presence of shoulders, based on the NMR spectra (see ESM, Fig. S9 and S10), we do not attribute them to the presence of an impurity.

IR spectroscopy of the azide ion has been widely studied. Frequency shifts and splittings of the ν_3 asymmetric stretching mode have been noted in a variety of circumstances. Wolfshorndl et al. [37] have noted for 5-azido-1-pentanoic acid, which is structurally related to **1**, a range of ν_3 frequencies from 2098 to 2110 cm^{-1} depending on the solvent used, with the appearance of shoulders in a couple of particular solvents. The authors observed that band asymmetry "is not apparently due to hydrogen bonding or any other intermolecular effect; rather, it is likely due to some underlying physical property of the vibration such as a weak Fermi resonance or other possible anharmonic complications...."

Solvent effect Alcohols are often used as solvents to bind polar organic molecules and biomolecules on nanostructured metal oxide films [38, 39]. For instance, in our previous work [26, 27], the binding of **1** and other COOH-substituted compounds on ZnO (and MgZnO) films was carried out using ethanol or 1-butanol solutions. However, we observed that the molecule/ZnO layer was not homogeneous [26], and considered the possibility that protic solvents, such as alcohols, may compete with the COOH group for binding. Here, we investigated the use of 3-methoxypropionitrile (MPN) a polar, non-protic solvent that is used in the electrolyte solution in dye-sensitized solar cells [40].

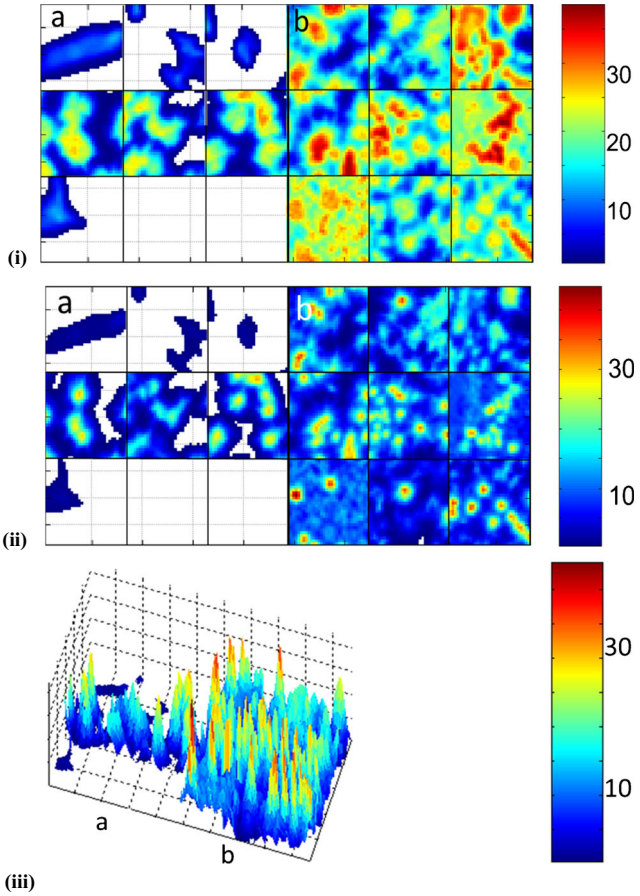

Fig. 2 FTIR images of the integrated band area of (**i**) the azide region 2212–2064 cm^{-1}(±STD), (**ii**) the carboxylate moiety region 1564–1480 cm^{-1} (±STD), and (**iii**) 3D 1564–1480 cm^{-1} (±STD) integrated areas of $MgZnO_{nano}$ films after binding with (**a**) 10 mM 11-azidoundecanoic acid (**1**) solution (solvent:2:1 1-butanol/ethanol) and (**b**) 10 mM 11-azidoundecanoic acid solution (solvent: MPN). The data were collected after 17 h binding

Comparisons were made between IR images of **1**/MgZnO films prepared from 10 mM solutions of **1** in 2:1 1-butanol/ethanol (Fig. 2(a)) and **1**/MgZnO films prepared from 10 mM solutions of **1** in MPN (Fig. 2(b)). These experiments were carried out using the same MgZnO film cut in half, to

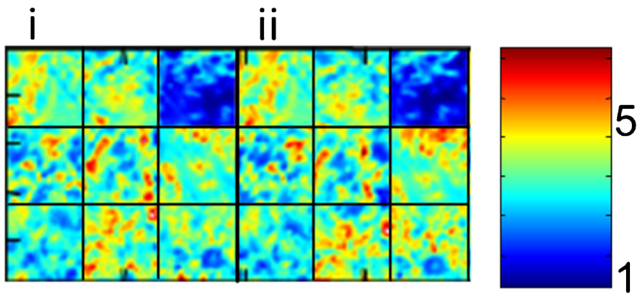

Fig. 3 Images of the integrated band area of 2212-2064 cm^{-1} (±STD) of a $MgZnO_{nano}$ film (**i**) after 64 h binding with **1** and (**ii**) after immersion of such functionalized film in ethanol solution at r.t for 24 h. The image (**i**) is shown in Fig. 4 (top, 64 h binding)

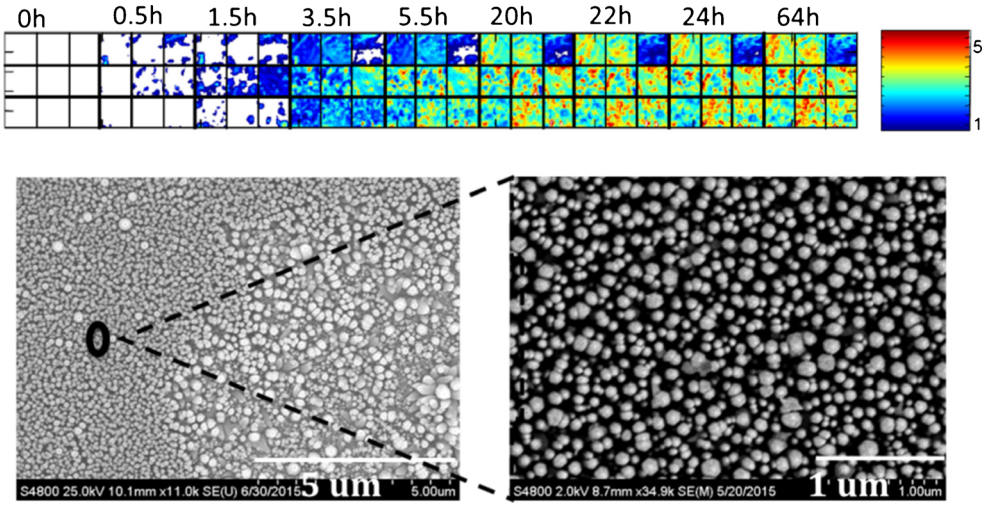

Fig. 4 *Top:* Images of the integrated band area of 2212–2064 cm^{-1} region (±STD) of $MgZnO_{nano}$ film before and after binding with a 10-mM 11-azidoundecanoic acid in MPN solution over time. *Bottom:* FESEM image of the $MgZnO_{nano}$ film used in the experiments (before binding) (left) and enlarged selected area (right). (Scale 5 μm left, 1 μm right)

minimize morphology differences and other differences between the samples used for the solvent effect comparison. The spectra were collected after 17 h binding time, and mapped as described in the "Experimental" Section. In addition, the images displayed in Fig. 2(i) and (ii) show the spatial distribution of the integrated area of the azide band (2212–2064 cm^{-1}) or carboxylate band (1564–1480 cm^{-1}) for the two solvents, respectively. A comparison of the **1**/MgZnO films formed using the two solvents (Fig. 2(a) vs (b)) clearly shows that by using MPN the surface coverage of **1** was largely improved. Also, a comparison of the IR images created using the azide versus the carboxylate moiety band area (Fig. 2(i) vs (ii)) consistently shows the same spatial distribution of both functional groups, indicating that neither the N_3 nor the COOH group independently physisorbs on the surface of the semiconductor. Seeing that the two spectral regions afforded similar IR images over time, in the following discussion we report IR images of the integrated area of the azide region, and provide the carboxylate moiety distribution in the Electronic Supplementary Material.

Based on the results obtained from the FTIR images in Fig. 2, we can infer that alcohols can compete during the binding of **1** onto $MgZnO_{nano}$ or displace the bound molecules of **1** during the binding process. Both processes could lead to lower binding coverage over the $MgZnO_{nano}$ film. However, we determined that the **1**/MgZnO layer, once formed from MPN, was chemically stable, and the immobilized **1** did not desorb after immersing the film in neat ethanol at r.t for 24 h, as shown in Fig. 3 (the 1564–1480 cm^{-1} region is shown in ESM Fig. S3). This observation is consistent with our prior observation that the functionalized film can be stable for further functionalization steps, including click reaction.

Binding time Figure 4, *top*, illustrates the distribution of **1** bound onto an $MgZnO_{nano}$ film imaged at different binding times, but from the same area. The IR images showed a

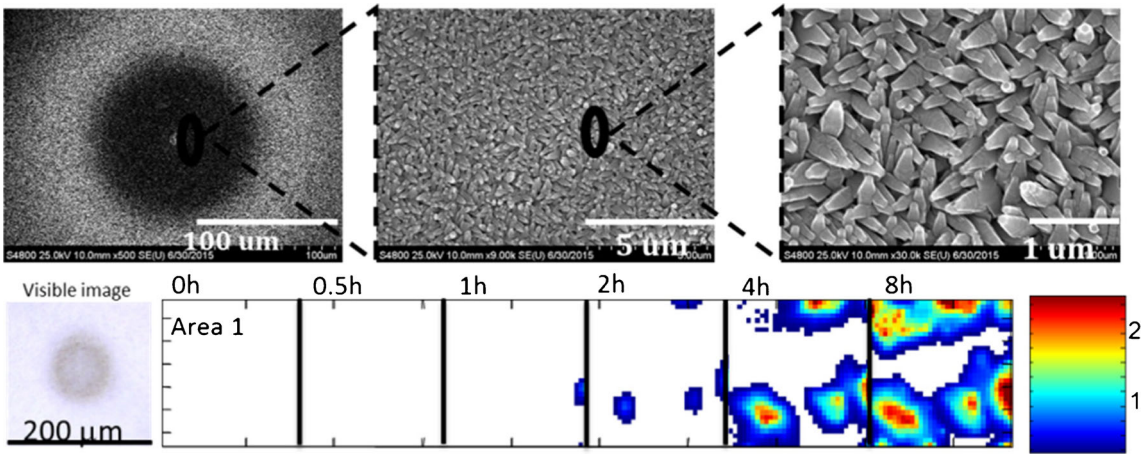

Fig. 5 SEM images of area 1 type morphology (before binding, top), and a visible micrograph (before binding, 200 × 200 μm^2) taken of the same area from which IR images were acquired as a function of binding time (bottom). IR images of the integrated band area, 2212–2064 cm^{-1} (±STD) of area 1 after binding with 10 mM 11-azidoundecanoic acid solution (solvent: MPN) as a function of time

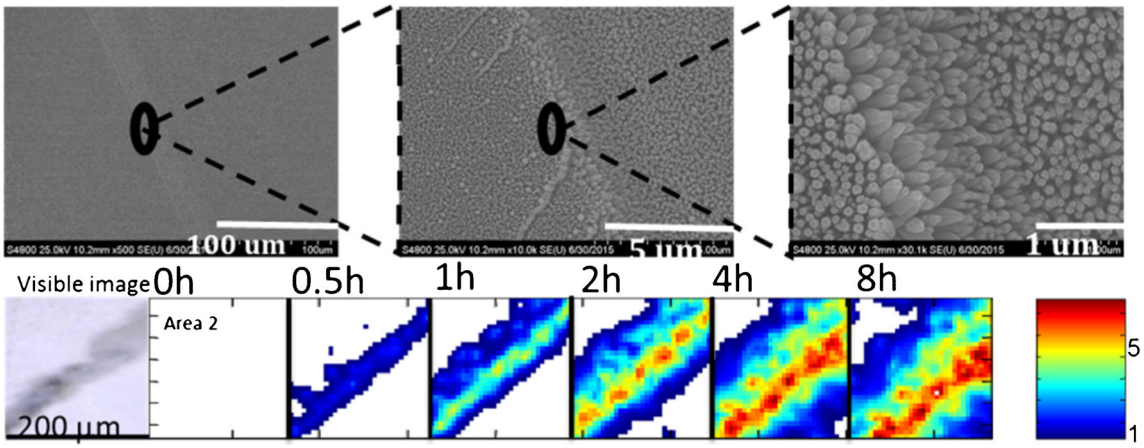

Fig. 6 SEM images of area 2 type morphology (before binding, top) and a visible micrograph (before binding, 200 × 200 μm^2) taken of the same area from which IR images were acquired as a function of binding time (bottom). IR images of the integrated band area of 2212–2064 cm^{-1} (±STD) of area 2 after binding with 10 mM 11-azidoundecanoic acid solution (**1**) (solvent: MPN) as a function of time

relatively fast binding rate within the first 5 h, and no changes in surface coverage after about 1 day. As shown in the full coverage FTIR image (i.e. > 24 h binding time), Fig. 4, top, the molecular layer bound on $MgZnO_{nano}$ was unevenly distributed. This is probably the result of growth heterogeneity often observed for $MgZnO_{nano}$ (or ZnO_{nano}) films, as evident by the SEM image of the pristine film used in the experiment (Fig. 4, *bottom*). Images of the integrated band area of the carboxylate moiety 1564–1480 cm^{-1} region are shown in ESM Fig. S4.

Close examination of IR images of the azido band area in two different regions of a $MgZnO_{nano}$ film at early binding times, show that binding starts in distinct, μm scale, islands that expand with time, and that finally merge together to form a full molecular layer (see ESM Fig. S5). This observation suggests that bound **1** may act as a "seed" inducing further binding of the 11-azidoundecanoic acid in solution, possibly though hydrophobic interactions of the long, saturated alkyl chains.

Morphology effect The SEM images (Fig. 4) indicate that the MOCVD-grown $MgZnO_{nano}$ films, in addition to areas with uniform, closely packed, vertically oriented nanorod arrays, also contained some non-uniform morphologies, including variations of the nanorod shape, different nanorod growth directions related to the substrate surface, or different nanorod density. We observed that such non-uniform area distribution influences the binding process, as suggested by SEM and FTIR images of the films following the binding of **1** (10 mM solutions in MPN).

As an example, we identified areas where $MgZnO_{nano}$ consists of sharp nanotips (Fig. 5, area inside the circle). Figure 5 clearly indicates little to no detectable binding in the area containing sharp nanotips at early binding times (0–2 h), and that **1** binds preferentially onto the uniform nanorod areas of the film (i.e., the area outside the circle) at later binding times (2–8 h).

We also probed binding in areas where the nanorods grow in different morphologies, including the shape, size, density, and particularly, growth directions of the nanorods, as shown in Fig. 6. The IR images in Fig. 6 indicate that binding is favored in this type of morphology, with faster binding rates at early binding times (0–1 h). Finally, ESM Fig. S8 highlights differences in the binding (after 2 h) for the two types of different morphologies shown in Figs. 5 and 6.

In summary, by using IR imaging, we consistently observed that morphology variations of the $MgZnO_{nano}$ films influence binding rates. A possible explanation is that different morphologies, especially different exposed faces of the MgZnO nanorods, have different binding energies, which impact the binding process [41]. Similar phenomena were observed when measuring the hydrophobicity in ZnO nanocrystal films with different morphologies.

Conclusions

MOCVD-grown $MgZnO_{nano}$ films were functionalized by reacting with solutions of **1**, a bifunctional linker. MgZnO was selected because it is more resistant to etching than ZnO whereas the low doping level (4 to 5% of MgO) ensures that selected properties useful for sensors development, such as piezoelectricity, are retained. This functionalization process was characterized by FTIR microscopic imaging, a method that, to our knowledge, has not been previously employed to characterize metal oxide films functionalization. The bound carboxylate moiety, as well as the azido end-group, were used as IR probes to monitor the distribution of 11-azidoundecanoic acid bound onto the films as a function of time and solvent used for the binding solution. We determined that protic solvents, such as alcohols, can compete during the

binding of 11-azidoundecanoic acid and largely decrease the amount of bound linker, but that alcohols can be used after the molecular layer has formed. By using polar, non-protic MPN the bound molecular layer's homogeneity, and the reproducibility of the binding experiments, dramatically improved. Also, we found that binding onto $MgZnO_{nano}$ film occurs first in μm-scale islands, then expand to form a rather uniform layer after 22 h. Areas of the $MgZnO_{nano}$ with uneven growth of the nanorod film influence the binding rate and molecular layer homogeneity. In summary, through the spatio-temporal analysis of the FTIR imaging of the binding of 11-azidoundecanoic acid to $MgZnO_{nano}$, we demonstrated the optimization of the binding coverage of a bifunctional linker to $MgZnO_{nano}$ through the COOH group.

Acknowledgements The authors gratefully acknowledge support of this research by the National Science Foundations through a NSF-CBET collaborative research grant (Grant Number 1264488) and NSF-CBET (Grant Number 1264508).

Compliance with ethical standards

Conflict of interest The authors declare that they have no conflicts of interests.

References

1. Niskanen M, Kuisma M, Cramariuc O, Golovanov V, Hukka TI, Tkachenko N, et al. Porphyrin adsorbed on the (1010) surface of the wurtzite structure of ZnO–conformation induced effects on the electron transfer characteristics. Phys Chem Chem Phys. 2013;15(40):17408–18.
2. Labat F, Ciofini I, Hratchian HP, Frisch M, Raghavachari K, Adamo C. First principles modeling of eosin-loaded ZnO films: a step toward the understanding of dye-sensitized solar cell performances. J Am Chem Soc. 2009;131(40):14290–8.
3. Persson P, Lunell S, Ojamäe L. Quantum chemical prediction of the adsorption conformations and dynamics at HCOOH-covered ZnO (1010) surfaces. Int J Quantum Chem. 2002;89(3):172–80.
4. Gonzalez-Valls I, Lira-Cantu M. Vertically-aligned nanostructures of ZnO for excitonic solar cells: a review. Energy Environ Sci. 2009;2(1):19–34.
5. Hakola H, Sariola-Leikas E, Efimov A, Tkachenko NV. Effect of hole transporting material on charge transfer processes in zinc phthalocyanine sensitized ZnO nanorods. J Phys Chem C. 2016;120(13):7044–51.
6. Song J, Kulinich SA, Yan J, Li Z, He J, Kan C, et al. Epitaxial ZnO nanowire-on-nanoplate structures as efficient and transferable field emitters. Adv Mater. 2013;25(40):5750–5.
7. Tian C, Zhang Q, Wu A, Jiang M, Liang Z, Jiang B, et al. Cost-effective large-scale synthesis of ZnO photocatalyst with excellent performance for dye photodegradation. Chem Commun. 2012;48(23):2858–60.
8. Mishra YK, Modi G, Cretu V, Postica V, Lupan O, Reimer T, et al. Direct growth of freestanding ZnO tetrapod networks for multifunctional applications in photocatalysis, UV photodetection, and gas sensing. ACS Appl Mater Interfaces. 2015;7(26):14303–16.
9. Kumar N, Dorfman A, Hahm J-I. Ultrasensitive DNA sequence detection using nanoscale ZnO sensor arrays. Nanotechnology. 2006;17(12):2875–81.
10. Zhou J, Gu Y, Hu Y, Mai W, Yeh P-H, Bao G, et al. Gigantic enhancement in response and reset time of ZnO UV nanosensor by utilizing Schottky contact and surface functionalization. Appl Phys Lett. 2009;94(19):191103–3.
11. Menzel A, Subannajui K, Güder F, Moser D, Paul O, Zacharias M. Multifunctional ZnO-nanowire-based sensor. Adv Funct Mater. 2011;21(22):4342–8.
12. Wang ZL. ZnO nanowire and nanobelt platform for nanotechnology. Mater Sci Eng R Rep. 2009;64(3):33–71.
13. Chandiran AK, Abdi-Jalebi M, Nazeeruddin MK, Grätzel M. Analysis of electron transfer properties of ZnO and TiO2 photoanodes for dye-sensitized solar cells. ACS Nano. 2014;8(3):2261–8.
14. Asbury JB, Hao E, Wang Y, Ghosh HN, Lian T. Ultrafast electron transfer dynamics from molecular adsorbates to semiconductor nanocrystalline thin films. J Phys Chem B. 2001;105(20):4545–57.
15. Bandara J, Tennakone K, Jayatilaka P. Composite tin and zinc oxide nanocrystalline particles for enhanced charge separation in sensitized degradation of dyes. Chemosphere. 2002;49(4):439–45.
16. Braid JL, Koldemir U, Sellinger A, Collins RT, Furtak TE, Olson DC. Conjugated phosphonic acid modified zinc oxide electron transport layers for improved performance in organic solar cells. ACS Appl Mater Interfaces. 2014;6(21):19229–34.
17. Huss AS, Bierbaum A, Chitta R, Ceckanowicz DJ, Mann KR, Gladfelter WL, et al. Tuning electron transfer rates via systematic shifts in the acceptor state density using size-selected ZnO colloids. J Am Chem Soc. 2010;132(40):13963–5.
18. Morkoç H, Özgür Ü. Zinc oxide: fundamentals, materials and device technology: John Wiley & Sons; 2008.
19. Briscoe J, Dunn S. Piezoelectric nanogenerators—a review of nanostructured piezoelectric energy harvesters. Nano Energy. 2015;14:15–29.
20. Emanetoglu NW, Gorla C, Liu Y, Liang S, Lu Y. Epitaxial ZnO piezoelectric thin films for saw filters. Mater Sci Semicond Process. 1999;2(3):247–52.
21. Ip K, Frazier RM, Heo YW, Norton DP, Abernathy CR, Pearton SJ, et al. Ferromagnetism in Mn- and Co-implanted ZnO nanorods. J Vac Sci Technol B Microelectron Nanometer Struct. 2003;21(4):1476.
22. Onodera A, Tamaki N, Jin K, Yamashita H. Ferroelectric properties in piezoelectric semiconductor $Zn_{1-x}M_xO$ (M=Li, Mg). Jpn J Appl Phys. 1997;36(Part 1, NO. 9B):6008–11.
23. Cao Y, Galoppini E, Reyes PI, Duan Z, Lu Y. Morphology effects on the biofunctionalization of nanostructured ZnO. Langmuir. 2012;28(21):7947–51.
24. Ruther RE, Franking R, Huhn AM, Gomez-Zayas J, Hamers RJ. Formation of smooth, conformal molecular layers on ZnO surfaces via photochemical grafting. Langmuir. 2011;27(17):10604–14.
25. Taratula O, Galoppini E, Wang D, Chu D, Zhang Z, Chen H, et al. Binding studies of molecular linkers to ZnO and MgZnO nanotip films. J Phys Chem B. 2006;110(13):6506–15.
26. Cao Y, Galoppini E, Reyes PI, Lu Y. Functionalization of nanostructured ZnO films by copper-free click reaction. Langmuir. 2013;29(25):7768–75.
27. Taratula O, Galoppini E, Mendelsohn R, Reyes PI, Zhang Z, Duan Z, et al. Stepwise functionalization of ZnO nanotips with DNA. Langmuir. 2009;25(4):2107–13.
28. Reyes PI, Zhang Z, Chen H, Duan Z, Zhong J, Saraf G, et al. A ZnO nanostructure-based quartz crystal microbalance device for biochemical sensing. IEEE Sensors J. 2009;9(10):1302–7.
29. Zhang Q, Saad P, Mao G, Walters RM, Correa MCM, Mendelsohn R, et al. Infrared spectroscopic imaging tracks lateral distribution in human stratum corneum. Pharm Res. 2014;31(10):2762–73.
30. Brenner TM, Flores TA, Ndione PF, Meinig EP, Chen G, Olson DC, et al. Etch-resistant Zn1-xMgxO alloys: an alternative to ZnO for

carboxylic acid surface modification. J Phys Chem C. 2014;118(24):12599–607.
31. Yang J, Lin Y, Meng Y. Effects of dye etching on the morphology and performance of ZnO nanorod dye-sensitized solar cells. Korean J Chem Eng. 2013;30(11):2026–9.
32. Torbrügge S, Ostendorf F, Reichling M. Stabilization of zinc-terminated ZnO (0001) by a modified surface stoichiometry. J Phys Chem C. 2009;113(12):4909–14.
33. Luo B, Rossini JE, Gladfelter WL. Zinc oxide nanocrystals stabilized by alkylammonium alkylcarbamates. Langmuir. 2009;25(22): 13133–41.
34. Ohtomo A, Kawasaki M, Koida T, Masubuchi K, Koinuma H, Sakurai Y, et al. MgxZn1−xO as a II–VI widegap semiconductor alloy. Appl Phys Lett. 1998;72(19):2466–8.
35. MacPhail R, Strauss H, Snyder R, Elliger C. CH stretching modes and the structure of n-alkyl chains. II: long, all-trans chains. J Phys Chem. 1984;88(3):334–41.
36. Snyder R, Strauss H, Elliger C. Carbon-hydrogen stretching modes and the structure of n-alkyl chains. 1. Long, disordered chains. J Phys Chem. 1982;86(26):5145–50.
37. Wolfshorndl MP, Baskin R, Dhawan I, Londergan CH. Covalently bound azido groups are very specific water sensors, even in hydrogen-bonding environments. J Phys Chem B. 2012;116(3): 1172–9.
38. Qu Q, Geng H, Peng R, Cui Q, Gu X, Li F, et al. Chemically binding carboxylic acids onto TiO2 nanoparticles with adjustable coverage by solvothermal strategy. Langmuir. 2010;26(12):9539–46.
39. Rossini JE, Huss AS, Bohnsack JN, Blank DA, Mann KR, Gladfelter WL. Binding and static quenching behavior of a terthiophene carboxylate on monodispersed zinc oxide nanocrystals. J Phys Chem C. 2011;115(1):11–7.
40. Boschloo G, Häggman L, Hagfeldt A. Quantification of the effect of 4-tert-butylpyridine addition to I-/I3-redox electrolytes in dye-sensitized nanostructured TiO_2 solar cells. J Phys Chem B. 2006;110(26):13144–50.
41. Mclaren A, Valdes-Solis T, Li G, Tsang SC. Shape and size effects of ZnO nanocrystals on photocatalytic activity. J Am Chem Soc. 2009;131(35):12540–1.